ELSEVIER

Cement & Concrete Composites 26 (2004) 551–562

Cement & Concrete Composites

www.elsevier.com/locate/cemconcomp

Chemoplastic material model for the simulation of early-age cracking: From the constitutive law to numerical analyses of massive concrete structures

Roman Lackner *, Herbert A. Mang

Institute for Strength of Materials, Vienna University of Technology, Austria, Karlsplatz 13/202, Vienna 1040, Austria

Abstract

This paper deals with the development and application of a three-dimensional material model for the simulation of early-age cracking of concrete. The starting point is the determination of the intrinsic material function for the fracture energy of early-age concrete. For this purpose, results of beam bending tests reported in [Proceedings of the SEM/RILEM International Conference on Fracture of Concrete and Rock. Houston, Texas, USA: 1987. p. 409] are employed. The intrinsic material function serves as input for the calibration of the Rankine fracture criterion formulated in the framework of chemoplasticity. Finally, the developed 3D material model is employed for a chemomechanical analysis of a roller-compacted-concrete dam. The temperature fields and the field of the degree of hydration required for this analysis are obtained from a preceding thermochemical analysis of the dam.

Keywords: Concrete; Chemoplasticity; Couplings; Cracking; Rankine criterion; Fracture energy; Intrinsic material function

1. Constitutive law for the simulation of early-age cracking of concrete

Over the last decade, numerous efforts have been undertaken to develop macroscopic material laws for the description of the mechanical behavior of early-age concrete. Beside rather empirical material models, as proposed in [1–3], material formulations on the basis of thermodynamics of chemically reactive porous media [4,5] have been applied to early-age concrete since the mid-1990s [6–8]. The theory of chemoplasticity was proposed in order to provide a sound chemo-physical basis for material laws for hydrating concrete. Hereby, the mechanical properties of concrete are related to the extent of the chemical reaction between cement and water by means of intrinsic material functions. These functions are obtained from extended laboratory tests.

The extension of material laws for early-age concrete to consideration of fracture was accomplished by means of a variable fracture energy in time (see, e.g., [2,9]). Respective experimental data showing the time-dependence of the fracture energy are given in [10,11].

This section deals with the determination of the intrinsic material function for the fracture energy. In the framework of chemoplasticity, this material function will be used for the calibration of a multisurface model, employing three (maximum stress) Rankine surfaces for the simulation of tensile failure of concrete. This model is briefly outlined in the following subsection (for details, see [8]).

1.1. Multisurface chemoplasticity model for concrete

The state of the chemical reaction between cement and water, termed hydration, is described macroscopically by means of a scalar variable, referred to as the degree of hydration ξ. This variable is obtained by relating the mass of reaction products per unit volume, m, to the mass of reaction products at the end of hydration, m_∞. Hence, $\xi = m/m_\infty$.

The evolution of ξ is described by means of an Arrhenius type law [4],

$$\dot{\xi} = \tilde{A} \exp\left(-\frac{E_a}{RT}\right), \tag{1}$$

* Corresponding author. Tel.: +43-1-58801-20224; fax: +43-1-58801-20299.

E-mail addresses: roman.lackner@tuwien.ac.at (R. Lackner), herbert.mang@tuwien.ac.at (H.A. Mang).

URL: http://www.fest.tuwien.ac.at.

0958-9465/$ - see front matter © 2003 Elsevier Ltd. All rights reserved.
doi:10.1016/S0958-9465(03)00071-4

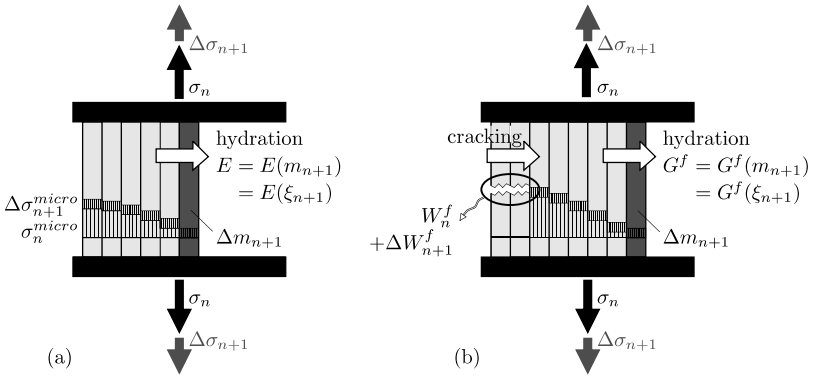

Fig. 1. 1D rheological model illustrating (a) the formation of new hydrates in a state free of microstress and (b) cracking of hydrates (m: specific mass of formed hydrates, σ^{micro}: microstress in the hydrates, σ: macroscopic stress, E: aging Young's modulus, G^f: aging fracture energy, W^f: released energy).

accounting for the thermally activated nature of the hydration process. In Eq. (1), T is the absolute temperature, E_a is the activation energy of the hydration process, and R is the universal constant for ideal gases with $R = 8315$ J/(mol K). According to [12], $E_a = 33\,500$ J/mol for $T \geqslant 293$ K and $E_a = 33\,500 + 1470 \times (293 - T)$ for $T < 293$ K. Throughout this paper, a constant value for E_a/R of 4000 K will be used. The chemical affinity $\tilde{A}$ is the driving force of the hydration reaction. Hence, it is responsible for changes of ξ. For concrete, $\tilde{A}$ depends mainly on ξ, which is expressed by the intrinsic material function $\tilde{A}(\xi)$.

ξ defines the mechanical properties of concrete. These chemomechanical couplings are reflected, e.g., by increasing strength $f_c(\xi)$ (chemical hardening) and stiffness $E(\xi)$ (aging elasticity).

Microcracking is described by means of the Rankine criterion, yielding the space of admissible stress states, C_E, in the form [8]

$$\boldsymbol{\sigma} \in C_E \Longleftrightarrow \begin{cases} f_{R1}(\sigma_1, \zeta) = \sigma_1 - \zeta(\xi) \leqslant 0, \\ f_{R2}(\sigma_2, \zeta) = \sigma_2 - \zeta(\xi) \leqslant 0, \\ f_{R3}(\sigma_3, \zeta) = \sigma_3 - \zeta(\xi) \leqslant 0, \end{cases} \tag{2}$$

where σ_A denotes the Ath principal stress. In [28], the hardening force ζ, which is associated with the size of the yield surface in the stress space, is assumed to depend only on the degree of hydration ξ (*pure* chemical hardening).

Assuming associative plasticity, the flow rule for the $(n+1)$st time (load) increment becomes [13]

$$\Delta\boldsymbol{\varepsilon}^p_{n+1} = \Delta\lambda_{R1,n+1}\frac{\partial f_{R1}}{\partial\boldsymbol{\sigma}} + \Delta\lambda_{R2,n+1}\frac{\partial f_{R2}}{\partial\boldsymbol{\sigma}} + \Delta\lambda_{R3,n+1}\frac{\partial f_{R3}}{\partial\boldsymbol{\sigma}}, \tag{3}$$

with the plastic multipliers λ_{R1}, λ_{R2}, and λ_{R3}.

During the chemical reaction of concrete, new hydrates are formed in a state which is free of microstress [14]. Hence, each hydrate is exclusively loaded by microstress resulting from macrostress applied *after* the formation of the respective hydrate (see Fig. 1(a)). This situation is accounted for by an incremental (as opposed to a total) stress–strain law [7], reading for the $(n+1)$st time (load) increment

$$\Delta\boldsymbol{\sigma}_{n+1} = \mathbf{C}_{n+1} : [\Delta\boldsymbol{\varepsilon}_{n+1} - \Delta\boldsymbol{\varepsilon}^p_{n+1} - \mathbf{1}\alpha_T\Delta T_{n+1}], \tag{4}$$

with $\mathbf{C}_{n+1}$ as the (aging) isotropic elasticity tensor, depending on Young's modulus $E(\xi_{n+1})$ and on a (constant) Poisson's ratio. α_T is the coefficient of thermal dilation, which is assumed to be constant. ΔT_{n+1} represents the temperature change in the $(n+1)$st time (load) increment and $\mathbf{1}$ is the second-order unity tensor.

In contrast to the formation of hydrates, at fracture they are loaded by microstresses (see Fig. 1(b)). This results in a macroscopically observable energy release, denoted as W^f. The amount of released energy related to cracking of all hydrates located in a unit area of the crack surface is the fracture energy, denoted as G^f. G^f increases in the course of the hydration process. This increase is described by means of an intrinsic material function, $G^f(\xi)$ (see, e.g., [10]). In the following subsection, the determination of $G^f(\xi)$ from experimental data will be described. For this purpose, experimental results obtained from bending beam tests and uniaxial compression tests are considered [11].

1.2. Determination of intrinsic material function for G^f, $G^f(\xi)$

Experimental results from beam bending tests and uniaxial compression tests of concrete at different ages are reported in [11]. The respective results for concrete characterized by a cement content of 315 kg PZ 35(F)/m^3 and a water /cement-ratio of 0.54 are listed in Table 1.

Determination of the intrinsic material function for the fracture energy, $G^f(\xi)$, is performed in two steps:

Table 1
Experimental results for compressive strength f_c and fracture energy G^f at different ages of concrete [11]

Age	f_c [N/mm^2]	G^f [N mm/mm^2]
4 h	0.1	0.0002
5 h	0.2	0.0010
6 h	0.4	0.0021
7 h	0.7	0.0053
8 h	2.6	0.0069
12 h	5.2	0.0190
24 h	13.8	0.0451
3 days	28.2	0.0625
7 days	31.7	0.0646
28 days	39.8	0.0652

(1) In the first step, the chemical affinity $\tilde{A}$ of the considered concrete is evaluated. It is computed from the given evolution of the compressive strength (see Table 1). Hereby, the chemomechanic coupling, which results in an increase of the compressive strength, is exploited. Experimental results [15–18] suggest linear chemical hardening, as illustrated in Fig. 2(a). In this figure, ξ_0 denotes the percolation threshold [19] beyond which the material can support a stress deviator. From this threshold on, the material strength is increasing linearly with increasing degree of hydration. Combining $f_c(t)$ given in Table 1 and $\xi(f_c)$ according to Fig. 2(a), yields the degree of hydration as a function of time:

$$\xi(t) = \xi[f_c(t)] = \xi_0 + (1-\xi_0)\frac{f_c(t)}{f_{c,\infty}}, \tag{5}$$

where $f_{c,\infty}$ is the final compressive strength.

Reformulation of Eq. (1) and use of Eq. (5) yields the chemical affinity as a function of time as

$$\tilde{A}(t) = \frac{d\xi(t)}{dt}\exp\left(\frac{E_a}{RT}\right) = \frac{1-\xi_0}{f_{c,\infty}}\frac{df_c(t)}{dt}\exp\left(\frac{E_a}{RT}\right). \tag{6}$$

Because of the small dimensions of the cylindrical specimens used for the compression tests (diameter: 75 mm, length: 150 mm), isothermal conditions are assumed for the evaluation of $\tilde{A}(t)$. According to [11], the specimens were stored at an environmental temperature of 23 °C. Hence, $T = 23$ °C. Based on Eqs. (5) and (6), $\xi(t)$ and $\tilde{A}[\xi(t)]$ are evaluated at certain time instants $t = t_i$ (see the circles in Fig. 2(b)). Performing a nonlinear regression analysis provides an analytical expression for the chemical affinity as depicted in Fig. 2(b).

(2) In the second step, the degree of hydration of the beam specimens is evaluated for the different time instants given in Table 1. In contrast to the cylindrical specimens used for the compression tests, the rather large dimensions of the beam (length × width × height = 500 × 120 × 112 mm) caused a considerable increase of temperature during hydration [11]. Fig. 3(a) shows the measured temperature at the center of a beam during the first 20 h [11]. For the remaining time interval from 20 h to 28 days the given temperature was extrapolated by means of a decaying exponential function. The asymptotic value of this function corresponds to the environmental temperature of 23 °C. The degree of hydration is obtained from integration of Eq. (1) using the chemical affinity given in Fig. 2(b) and the temperature evolution given in Fig. 3(a). Combination of the obtained values for ξ and the values for the fracture energy given in Table 1 gives direct experimental access to the intrinsic material function $G^f(\xi)$ for the considered concrete (see Fig. 3(b)). Regression analysis using a linear relation between the fracture energy and the degree of hydration shows good agreement with the experimental results. The correlation coefficient was found as 99.5%.

1.3. Consideration of fracture in the framework of chemoplasticity

In case of consideration of fracture of concrete, the hardening force ζ is not only dependent on the degree of hydration ζ (chemical hardening), but also on the hardening variable χ (strain-softening). Accordingly, in contrast to (2) [8], the definition of the space of admissible stress states C_E becomes

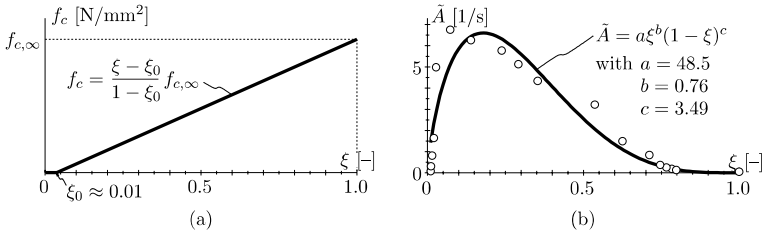

Fig. 2. Evaluation of the intrinsic material function for the chemical affinity, $\tilde{A}(\xi)$: (a) assumed linear relation between f_c and ξ, and (b) intrinsic material function $\tilde{A}(\xi)$.

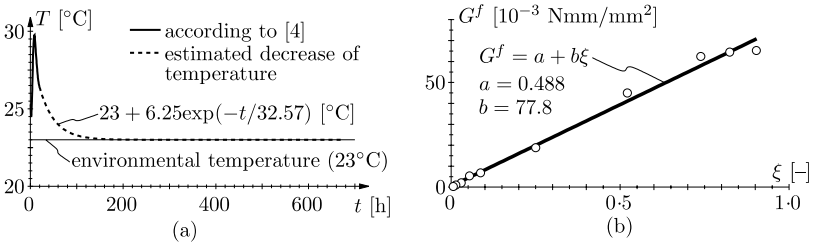

Fig. 3. Evaluation of the intrinsic material function for the fracture energy, $G^f(\xi)$: (a) temperature evolution at the center of the beam specimen and (b) intrinsic material function $G^f(\xi)$.

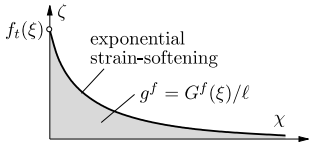

Fig. 4. Strain-softening curve of the Rankine criterion (f_t: tensile strength, with $f_t(\xi) = f_c(\xi)/10$).

$$\boldsymbol{\sigma} \in C_E \Longleftrightarrow \begin{cases} f_{R1}(\sigma_1, \zeta) = \sigma_1 - \zeta(\chi, \xi) \leqslant 0, \\ f_{R2}(\sigma_2, \zeta) = \sigma_2 - \zeta(\chi, \xi) \leqslant 0, \\ f_{R3}(\sigma_3, \zeta) = \sigma_3 - \zeta(\chi, \xi) \leqslant 0, \end{cases} \tag{7}$$

where χ is a strain-like internal variable accounting for the decrease of strength in consequence of plastic deformations. In the present material model, an exponential strain-softening curve is employed (see Fig. 4). Assuming associative hardening plasticity, the evolution law for χ becomes for the $(n+1)$st time (load) increment

$$\Delta\chi_{n+1} = \Delta\lambda_{R1,n+1}\frac{\partial f_{R1}}{\partial\zeta} + \Delta\lambda_{R2,n+1}\frac{\partial f_{R2}}{\partial\zeta} + \Delta\lambda_{R3,n+1}\frac{\partial f_{R3}}{\partial\zeta} \tag{8}$$

In general, softening introduces a dependence of the numerical results on the finite element discretization. Hence, a regularization of the numerical solution is required. In this paper, the fracture energy concept [20] is employed. It is characterized by setting the area under the softening curve, g^f, equal to G^f/ℓ, where the so-called characteristic length ℓ is related to the size of the respective finite element.

The intrinsic material function for the fracture energy, $G^f(\xi)$, was computed from experimental data given in the previous subsection. These tests were performed on originally uncracked specimens at certain time instants. In general, however, cracking and hydration are occurring simultaneously.

Hydration of the hitherto unhydrated cement results in the regaining of strength of cracked concrete, referred to as autogenous healing. It is the higher, the younger the concrete is, i.e., the more unhydrated cement it contains. According to [21], pressure acting on the crack faces assists autogenous healing. In this paper, however, the influence of the deformation and stress state on the increase of material properties in the course of the hydration process is not accounted for (partial decoupling hypothesis). Accordingly, the increase of the fracture energy G^f is not effected by cracking. Consequently, at the time $t = t_{n+1}$ the fracture energy is obtained from the degree of hydretion, reading $G^f_{n+1} = G^f(\xi_{n+1})$. In case of fracture of all hydrates formed so far at a crack face at $t = t_{n+1}$, the released energy W^f_{n+1} must be equal to the fracture energy G^f_{n+1}:

$$W^f_{n+1} := \ell\int_0^\infty \sigma\,\mathrm{d}\chi \overset{!}{=} G^f_{n+1} = G^f(\xi_{n+1}). \tag{9}$$

1.4. ID benchmark problem

A 1D benchmark problem is chosen to show that the numerical results obtained on the basis of the commonly used total formulation of the state equation for the hardening force ζ (see Fig. 4),

$$\zeta_{n+1} = \zeta_{n+1}(\chi_{n+1}, \xi_{n+1}) = f_t(\xi_{n+1})\exp\left(-\frac{\chi_{n+1}}{\bar{\chi}_{n+1}}\right), \tag{10}$$

do not satisfy condition (9). The term "total" reflects the dependence of ζ_{n+1} on the hardening variable χ at the time instant t_{n+1}, χ_{n+1}. In Eq. (10), $\bar{\chi}_{n+1}$ is a calibration parameter. It is obtained from setting the area under the exponential softening law (10) equal to $G^f(\xi_{n+1})/\ell$. Integration of Eq. (10) and reformulation yields the calibration parameter as

$$\bar{\chi}_{n+1} = \frac{G^f(\xi_{n+1})}{\ell f_t(\xi_{n+1})}. \tag{11}$$

For this benchmark problem, isothermal conditions ($T = 20$ °C) are assumed.

The considered benchmark problem consists of a cube ($0.1 \times 0.1 \times 0.1$ m), which is loaded uniaxially according to the following procedure: 20 h after casting a displacement of 0.03 mm, normal to two opposite faces is prescribed and kept constant for 80 h. Then, this displacement is increased. The cube is discretized by means of one cubic finite element. Hence, the characteristic length ℓ is equal to 100 mm. The employed material properties are given in Table 2. The increase of the tensile strength is controlled by means of the intrinsic material function depicted in Fig. 2(a), with $f_t(\xi) = f_c(\xi)/10$. According to Fig. 3(b), a linear relation

Table 2
1D benchmark problem: material properties

Final Young's modulus E_∞ [N/mm^2]	10 000
Poisson's ratio ν [–]	0.1
Final compressive strength $f_{c,\infty}$ [N/mm^2]	10.0
Final fracture energy G^f_∞ [N mm/mm^2]	0.025
Chemical affinity $\tilde{A} = a\xi^b(1-\xi)^c : a, b, c$	48.5, 0.76, 3.49

between the fracture energy and the degree of hydration is used, reading $G^f(\xi) = \xi G^f_\infty$.

Based on the assumed isothermal conditions and the chemical affinity given in Table 2, a preceding thermo-chemical analysis resulted in $\xi(t = 20) = 0.44$ and $\xi(t = 100) = 0.76$. The softening curves corresponding to $\xi = 0.44$ and 0.76 are depicted in Fig. 5 (dashed lines).

Fig. 5(a) shows the obtained results on the basis of the total formulation (10). The released energy $\mathscr{W}^f$ is computed as

$$\mathscr{W}^f = \ell w^f = \ell \int_0^\infty \sigma \, \mathrm{d}\chi = 0.013 \ \mathrm{N\,mm/mm^2}. \tag{12}$$

As expected, $\mathscr{W}^f$ obtained from the total formulation does not coincide with the respective fracture energy for $\xi = 0.61$, given by

$$G^f(\xi = 0.76) = \xi G^f_\infty = 0.76 G^f_\infty = 0.019 \ \mathrm{N\,mm/mm^2}. \tag{13}$$

Hence, condition (9) is violated.

The numerical results obtained from an incremental formulation of the state equation for the hardening for ζ, proposed as

$$\zeta_{n+1} = \zeta_{n+1}(\zeta_n, \Delta\chi_{n+1}, \Delta\xi_{n+1}) = [\zeta_n + \Delta\zeta^{\mathrm{hyd}}_{n+1}(\Delta\xi_{n+1})] \exp\left(-\frac{\Delta\chi_{n+1}}{\bar{\chi}_{n+1}}\right), \tag{14}$$

with

$$\bar{\chi}_{n+1} = \frac{G^f(\xi_{n+1}) - \mathscr{W}^f_n}{\ell[\zeta_n + \Delta\zeta^{\mathrm{hyd}}_{n+1}(\Delta\xi_{n+1})]}, \tag{15}$$

satisfy condition (9), i.e., $\mathscr{W}^f = \ell w^f = 0.019$ N mm/mm^2 (see Fig. 5(b)). In Eqs. (14) and (15), $\Delta\zeta^{\mathrm{hyd}}_{n+1}$ represents the increase of strength in consequence of chemical hardening. In contrast to the total formulation, this increase is added to ζ_n, which corresponds to the tensile strength at the beginning of the considered time (load) increment $n + 1$.

In order to assess crack opening in the context of the incremental formulation (14), a crack indicator C is introduced in the form

$$C = \frac{\mathscr{W}^f}{G^f(\xi)} \quad \text{with } 0 \leqslant C \leqslant 1. \tag{16}$$

C relates the released energy in consequence of cracking, $\mathscr{W}^f$, to the fracture energy G^f. Hence, for values of C equal to zero, no cracking has occurred so far. For $C = 1$, all hydrates at the crack face are broken, giving a tensile strength equal to zero. Fig. 6 shows the evolution of the crack indicator obtained from the considered benchmark problem. According to definition (16), the crack indicator depends on both the released energy $\mathscr{W}^f$ and, via the fracture energy, on the degree of hydration. Whereas cracking results in a increase of C, the formation of new hydrates in the course of the hydration process yields a reduction of C. Accordingly, during the 80 h break of loading at $\bar{u} = 0.03$ mm a reduction of C from 67% to 38% is observed in Fig. 6.

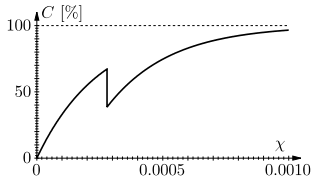

Fig. 6. 1D benchmark problem: C–χ curve obtained from incremental formulation (14).

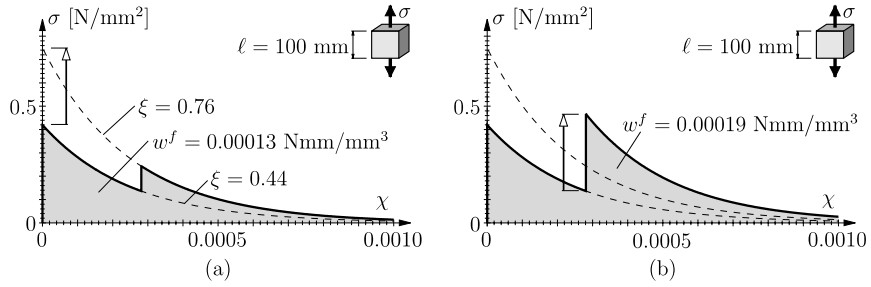

Fig. 5. 1D benchmark problem: σ–χ curve obtained from (a) a total and (b) an incremental formulation of the state equation for the hardening variable ζ ($w^f = \mathscr{W}^f/\ell$, with $\ell = 100$ mm and $\mathscr{W}^f$: released energy; dashed lines refer to continuous loading of concrete with $\xi = 0.44$ and 0.76, respectively).

2. Numerical analysis of massive concrete structures

The developed 3D material model for the simulation of early-age cracking of concrete has been applied in the context of thermochemomechanical analysis of a dam made of roller-compacted concrete (RCC). Accounting for the negligible influence of mechanical quantities on chemical and thermal processes (partially decoupling hypotheses), the analysis can be split into a thermochemical analysis and a subsequent chemomechanical analysis. Results of the thermochemical analysis are the temperature field and the field of the hydration degree. They serve as input for the chemomechanical analysis. Results of both the thermochemical and the chemomechanical analysis of the RCC dam will be presented in this section.

2.1. Introductionary remarks on RCC dams

The development of RCC dams started approximately three decades ago. Structural engineers (involved with concrete-dam design) together with geotechnical engineers (traditionally involved with embankment-dam design) were trying to combine the best features of both major types of dams. The so-obtained RCC dam exhibits the safety and maintenance advantages of concrete dams and the low cost and high production rates of earth or rockfill embankments. Today, about 200 RCC dams have been constructed all over the world [22]. The two main reasons for the wide acceptance of RCC dams are the simple design and construction concept, easily understood by the designer of both concrete dams and embankment dams, and the lower cost as compared to the two mentioned types of dams. The latter results from the reduction of the construction time and the material costs (the amount of cement required is less than that for conventional concrete; it is possible to use less costly aggregates; cooling pipes are not required).

According to [23], RCC is defined as a no-slump concrete compacted by vibratory rollers. It can be classified with respect to its cementitious content (including cement and pozzolan) into (see, e.g., [24])

- low-paste RCC characterized by a cementitious content lower than 100 kg/m^3, of which up to 40% can be pozzolan;
- medium-paste RCC which has a cementitious content between 100 and 150 kg/m^3; and
- high-paste RCC which is characterized by a cementitious content usually increasing 150 kg/m^3. However, in general 60–80% of the cementitious material is pozzolan.

Depending on the cementitious content and the amount of fine aggregates, the water content ranges from 90 to 130 l/m^3 [25]. This allows placing of RCC by earthmoving equipment and compaction with vibrating rollers. According to [25], the amount of the mentioned fine aggregate should, in general, increase 10% in order to guarantee sufficient compactibility and impermeability.

The motivation for the present analysis is to assess the temperature evolution in an RCC dam. In general, the cooling and, hence, the contraction of RCC is the main source for high tensile loading and cracking. The undesirable consequence of cracking in a dam is leakage through the dam or into the dam from the foundations. The problem with leakage is not so much its quantity provided it is in the "normal range" for dams, but its invisibility. Moreover, occasionally leakage causes internal erosion. Repair can be expensive, particularly if the reservoir cannot be emptied.

2.2. Geometric dimensions, construction history, and finite element (FE) discretization

The geometric dimensions of the considered RCC dam are given in Fig. 7. The total height of the dam is

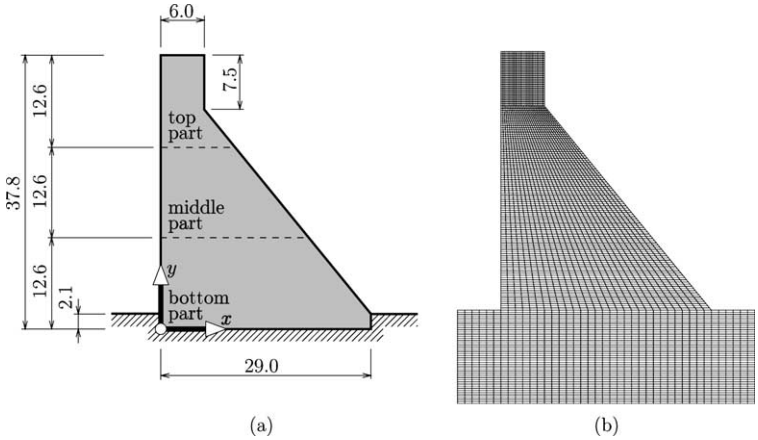

Fig. 7. RCC dam: (a) geometric dimensions (in [m]) and (b) FE mesh consisting of 5214 finite elements.

Table 3
Construction performance for different parts of the RCC dam

Construction phase	Elevation		Performance [layer(s)/day]
	From [m]	To [m]	
Bottom part	0.0	12.6	1
Middle part	12.6	25.2	2
Top part	25.2	37.8	3

37.8 m. It is constructed by means of 126 layers of RCC. Each layer has a thickness of 0.3 m. The time assigned to the installation of one layer was adjusted to the actual thickness of the dam (see Table 3). The installation of one layer of RCC at the bottom part of the dam (see Fig. 7(a)) is assumed to take 24 h. In the same time span, two layers are installed in the middle part of the dam. Finally, for the top part of the dam, the construction speed is increased to three layers per day.

The dam and the surrounding rock are discretized by means of four-node finite elements. The FE mesh used for both the thermochemical and the chemomechanical analysis is shown in Fig. 7(b). The height of each element was set equal to the thickness of the RCC layers, i.e., 0.3 m.

2.3. Solution of the thermochemical problem

The field equation of the thermochemical problem is derived from the first law of thermodynamics. In the absence of volume heat sources and of negligible terms such as e.g. the heat release in consequence of deformations, this law is given as [4]

$$\rho c\dot{T} - \ell_\xi \dot{\xi} = -\text{div}\ \mathbf{q}, \tag{17}$$

with ρ [kg/m^3] as the density, c [kJ/(kg K)] as the specific heat capacity, and ℓ_ξ [kJ/m^3] as the heat of hydration per unit volume of RCC. $\mathbf{q}$ is the heat flow vector. It is related to the temperature T via Fourier's linear (isotropic) heat conduction law,

$$\mathbf{q} = -k\ \text{grad}\, T, \tag{18}$$

with k [kJ/(m h K)] as the thermal conductivity. The field equation (17) accounts for the release of the latent heat ℓ_ξ resulting in an increase of the temperature in the course of hydration. The influence of the temperature on the chemical reaction between cement and water, on the other hand, is considered by the Arrhenius law (1).

The latent heat associated with the hydration of 1 m^3 RCC characterized by a cementitious content of 90 kg/(m^3 RCC) (low-paste RCC with a water/cement ratio of 1.0, in the following referred to as "RCC 90") is estimated from

$$\ell_\xi = 90 \times 500 = 45\,000\ \text{kJ}/(\text{m}^3\ \text{RCC}), \tag{19}$$

where 500 kJ/kg represents the latent heat of 1 kg cementitious material. The chemical affinity $\tilde{A}(\xi)$ of the employed RCC 90 was computed on the basis of adiabatic tests reported in [26]. In addition to RCC 90, an RCC with lower cementitious content, characterized by a cementitious content of 60 kg/(m^3 RCC) and a water/cement-ratio of 1.6, was considered in [26]. The parameters of the employed affinity functions, a, b, and c, are determined from the adiabatic tests of both RCCs (see Fig. 8(b)). The temperature histories are plotted in Fig. 8(b). They correspond to the chemical affinity $\tilde{A}(\xi)$ depicted in Fig. 8(a). Good agreement between experimental and numerical results is observed. The material parameters employed in the thermochemical analysis are summarized in Table 4.

The initial temperatures T_0 of RCC and rock are 20 °C and 10 °C, respectively. At the RCC-air and the rock-air boundary of the numerical model, the heat flux q_n is prescribed as

$$q_n = \alpha_R (T - T^\infty) \tag{20}$$

Table 4
Material properties of RCC [26] and rock [27] used in the thermochemical analysis

	RCC 90	Rock
Density ρ [kg/m^3]	2500	2610
Heat capacity c [kJ/(kg K)]	1.0	0.937
Thermal conductivity k [kJ/(m h K)]	6.11	11.84
Latent heat (RCC 90) ℓ_ξ [kJ/(m^3 RCC)]	45 000	–
Chemical affinity $\tilde{A} = a\xi^b(1-\xi)^c$; a, b, c:	57.0, 0.75, 7.05	–

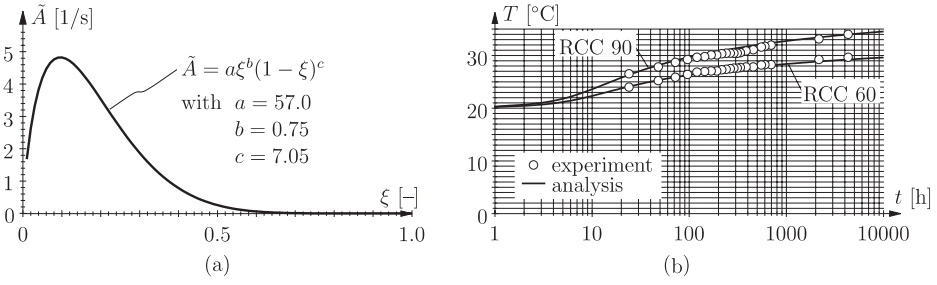

Fig. 8. Determination of $\tilde{A}(\xi)$ from adiabatic tests: (a) function obtained for $\tilde{A}$ and (b) temperature values from adiabatic experiments [26] and numerically obtained temperature histories.

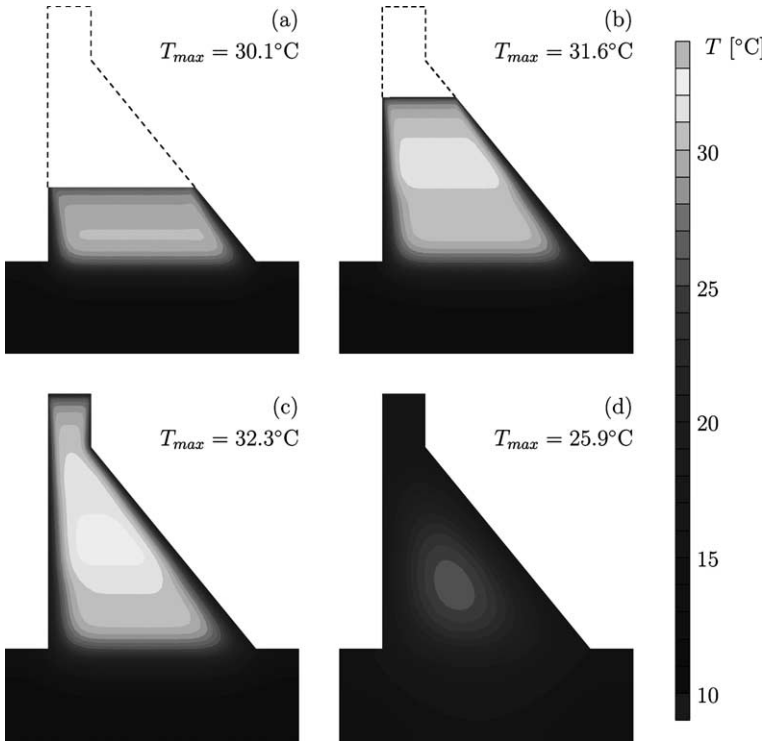

Fig. 9. Thermochemical analysis: temperature distribution at the end of the different construction phases, i.e., at (a) $t = 42$ days, (b) $t = 63$ days, and (c) $t = 77$ days; (d) temperature distribution at $t = 483$ days.

where α_R is the respective radiation coefficient. T^∞ is the environmental temperature. In the present analysis, T^∞ is set equal to 15 °C. The radiation coefficients are taken from the open literature as $\alpha_R = 14.4$ kJ/(h m^2 K) for the RCC–air interface [28] and as $\alpha_R = 72$ kJ/(h m^2 K) for the rock–air interface [29].

Fig. 9 shows the distribution of the temperature at four different instants of time. The maximum possible temperature rise in the course of hydration can be estimated by specializing the field equation of the thermochemical problem for adiabatic conditions obtained by setting div $\mathbf{q}$ in (17) equal to 0:

$$\rho c \Delta T_{\max} - \ell_\xi = 0, \tag{21}$$

where $\xi(t = \infty) = 1$ was considered. Based on the material properties given in Table 4, $\Delta T_{\max}$ becomes equal to 18 °C. The maximum temperature shown in Fig. 9, however, is approximately 5 °C lower than the temperature referring to adiabatic conditions $T = T_0 + \Delta T_{\max} = 20 + 18 = 38\ °C$. Hence, a considerable part of the latent heat leaves the dam. This occurs mainly through the top surface which is characterized by the largest difference $T - T^\infty$ (see Eq. (20)). Accordingly, an increase of the construction speed provides less time for temperature radiation, explaining the higher temperatures observed at the middle and top parts of the dam (see Fig. 9(b) and (c)). 483 days after the installation of the first RCC layer, i.e., 406 days after the end of the construction of the dam, the maximum temperature in the dam is still 25.9 °C (see Fig. 9(d)).

The respective distributions of the degree of hydration ξ are shown in Fig. 10. The horizontal lines separating different values of ξ in Fig. 10(a) and (b) indicate, apart from the areas close to the side walls of the dam, a uniform distribution of ξ across the thickness of the dam. This observation underlines the previous statement that a significant part of the latent heat leaves the dam mainly through the top surface. This results in a uniform distribution of the temperature across the thickness of the dam and, hence, through the Arrhenius law (1) in a uniform distribution of ξ. The influence of radiation at the side walls of the dam results in slightly lower values of ξ in the area of a layer close to the side walls. At $t = 483$ days (Fig. 10(d)), hydration is still in progress. The largest values of ξ are found in the center of the dam.

The obtained distributions of the temperature and the degree of hydration serve as input for the following chemomechanical analysis.

2.4. Solution of the chemomechanical problem

In order to assess the influence of temperature changes during the hydration process on the stress state in the dam, neither chemical shrinkage nor short-term and long-term creep (see, e.g., [8]) are considered in the

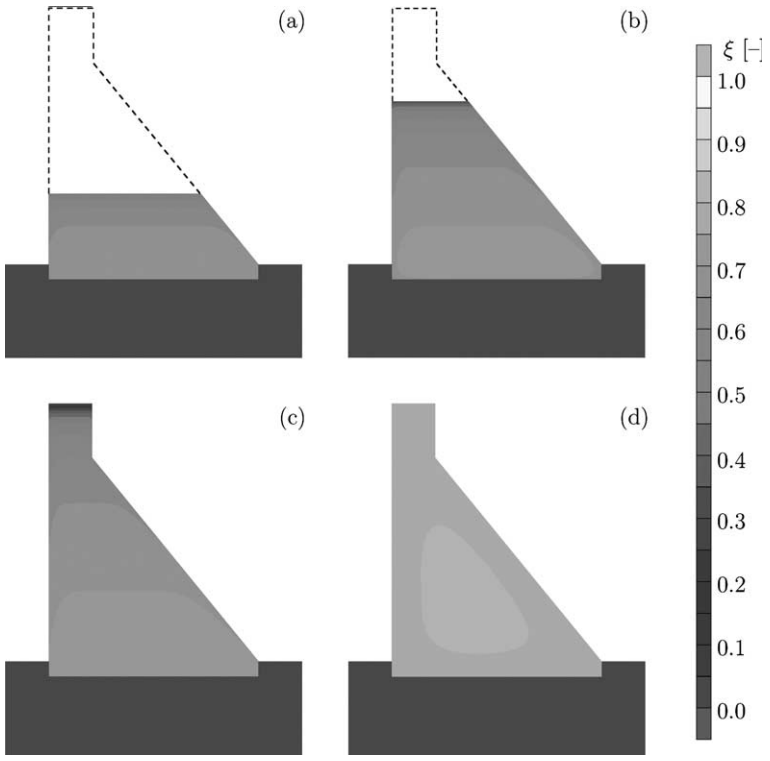

Fig. 10. Thermochemical analysis: distribution of the degree of hydration ξ at the end of the different construction phases, i.e., at (a) $t = 42$ days, (b) $t = 63$ days, and (c) $t = 77$ days; (d) distribution of ξ at $t = 483$ days.

Table 5
Material properties of RCC [26] and rock [27] used in the chemomechanical analysis

	RCC 90	Rock
Young's modulus E [N/mm^2]	22 000	10 000
Poisson's ratio v [–]	0.15	0.15
Uniaxial compressive strength $f_{c,\infty}$ [N/mm^2]	13.6	–
Thermal dilation coefficient α_T [1/°C]	8.33×10^{-6}	3.0×10^{-6}

present analysis. Hence, the stresses obtained from the following analysis are resulting from dead load of RCC and from temperature changes *only*.

The material properties used for RCC and the surrounding rock are given in Table 5. In contrast to Poisson's ratio v and the thermal dilation coefficient α_T which are assumed to be constant during the analysis, Young's modulus E and the uniaxial compressive strength f_c of RCC depend on the degree of hydration. The respective intrinsic material functions relating E and f_c to the degree of hydration are depicted in Fig. 11. According to [30], the tensile strength of RCC is 10–15% of its compressive strength. Herein, the tensile strength f_t was chosen as $f_t(\xi) = 0.1 f_c(\xi)$. The fracture energy at complete hydration, G_∞^f was set equal to 0.06 N mm/mm^2.

Fig. 12 shows the distributions of the horizontal and the vertical in-plane stress component and of the out-of-plane component at the end of the construction of the RCC dam, i.e., at $t = 77$ days. Tensile stresses prevail at the dam–rock interface and at the downstream face of the dam. As regards the out-of-plane stress component, σ_z, tensile stresses are observed at the bottom and along

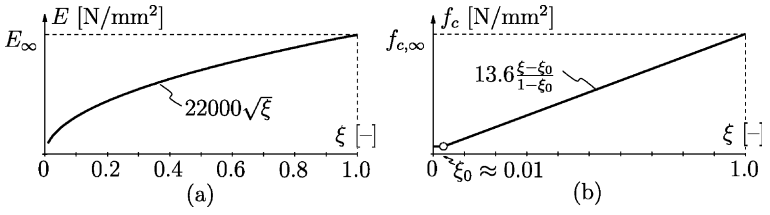

Fig. 11. Chemomechanical analysis: intrinsic material functions for (a) Young's modulus E and (b) the uniaxial compressive strength f_c.

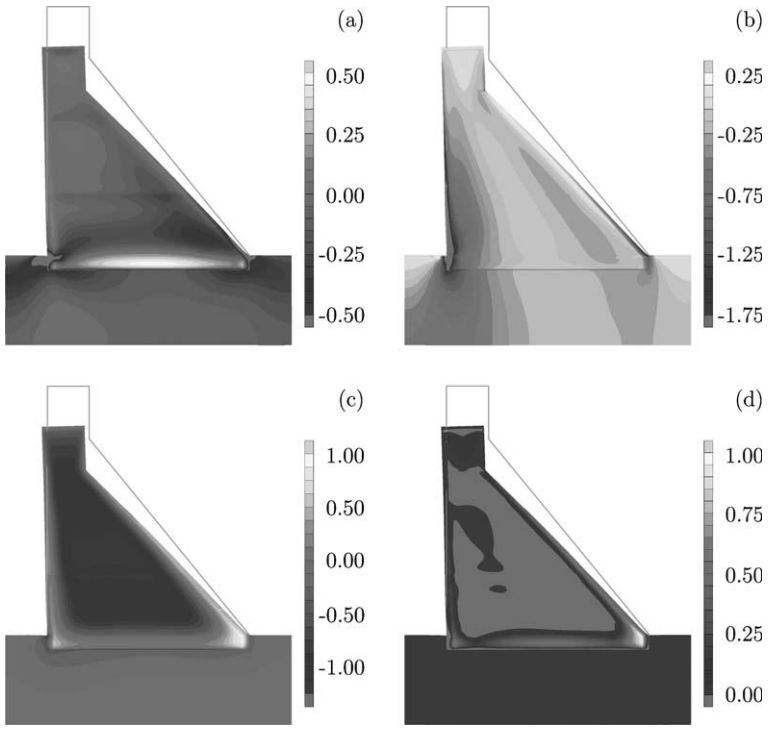

Fig. 12. Chemomechanical analysis with $T^{\infty} = 15$ °C and $\ell_{\xi} = 45000$ kJ/(m^3 RCC): distribution of (a) σ_x, (b) σ_y, (c) σ_z, and (d) L at $t = 77$ days (100-fold magnification of displacements).

the side faces of the dam. Because of its geometric properties, the dam leans towards its upstream side, resulting in compressive vertical stresses at the upstream face of the dam. However, neither the in-plane stresses nor the out-of-plane component have caused cracking of RCC. This reflects the quality of the design of the dam aimed at minimization of cracking. In order to assess the risk of cracking, the level of loading L is introduced as $L = \sigma_1/f_t(\xi)$. $L = 0$ refers to a situation with no loading of RCC. At $L = 1$, the tensile strength of RCC is reached and cracking is initiated. Fig. 12(d) shows the distribution of L at $t = 77$ days. The maximum value of L was found to be 91%. The distribution of the level of loading confirms previous statements regarding the stress distribution in the dam. Levels of loading up to 58% are observed at the bottom and the downstream face of the dam. The peak value of 91% was found at the bottom of the downstream face of the dam stemming from high tensile loading in the longitudinal direction (see Fig. 12(c)).

In order to assess the performance of the proposed material model for the simulation of early-age cracking of concrete, a second analysis was performed. Now, however, the environmental temperature T^{∞} was reduced from 15 to 5 °C. Moreover, the cementitious content in the RCC was increased from 90 to 200 kg/(m^3 RCC), giving a latent heat of $\ell_{\xi} = 100000$ kJ/(m^3 RCC). The increase of ℓ_{ξ} resulted in higher temperatures in the dam obtained from the preceding thermochemical analysis. E.g., the maximum temperature in the dam at $t = 77$ days increased from 32.3 °C for the original design (see Fig. 9(c)) to 47.4 °C. The increased temperature of the dam and the reduction of T^{∞} resulted in an increase of the temperature gradients. Accordingly, cracking was encountered in the corresponding chemomechanical analysis. Fig. 13(a) shows the regions characterized by $\chi > 0$ and, hence, by cracking of RCC. Cracking is observed at the bottom and the side faces of the dam. Moreover, a significant part of the interior of the dam experienced cracking. This is a consequence of unequal settlements of the dam. In the center of the dam, the temperature increase in the rock and in the RCC gave smaller settlements resulting in tensile loading at the top of the dam corresponding to the respective construction state. At the region indicated in Fig. 13(a), the tensile stresses exceeded the tensile strength of early-age RCC. The crack indicator C (see Eq. (16)) gives insight into the extent of cracking. Fig. 13(b) reveals that the main part of the dam is characterized by a low level of C, indicating that most cracks opened at early age of RCC and, hence, healed in the course of the hydration process. According to the obtained numerical results, the largest extent of cracking can be expected at the downstream face of the dam.

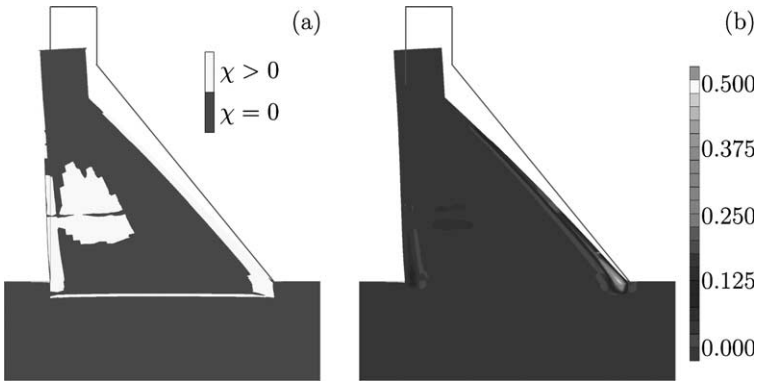

Fig. 13. Chemomechanical analysis with $T^{\infty} = 5$ °C and $\ell_{\xi} = 100\,000$ kJ/(m^3 RCC): (a) regions with cracking of RCC ($\chi > 0$) and (b) distribution of C at $t = 77$ days (100-fold magnification of displacements).

3. Concluding remarks

In this paper, a 3D material model for the simulation of early-age cracking of concrete was proposed. It was based on the Rankine criterion formulated in the framework of multisurface chemoplasticity. An incremental formulation of the state equation for the hardening force of the Rankine criterion was proposed. In contrast to the incremental formulation, use of the total formulation resulted in an underestimation of the released energy during cracking and in an underestimation of the regained strength in consequence of crack healing in the course of the hydration process. The incremental formulation, on the other hand, gave the correct result. The softening function appearing in the model formulation was calibrated by means of the fracture energy concept. The required intrinsic material functions for the fracture energy was determined from experimental results reported in [11]. This function was found to increase almost linearly with the degree of hydration.

The proposed 3D material model was applied to the analysis of an RCC dam. Prior to the chemomechanical analysis, a thermochemical analysis was performed. From the temperature fields and the fields of the degree of hydration obtained from the thermochemical analysis, the following conclusions can be drawn:

- Whereas adiabatic conditions would have resulted in a temperature rise of 18 °C, the maximum temperature rise in the dam was 13 °C. A significant part of the latent heat left the dam through the top surface by means of radiation.
- Within each layer, an almost uniform temperature distribution was obtained.
- 406 days after termination of the construction of the dam, the hydration process was still in progress. At this time instant, the temperature in the center of the dam was 25.9 °C.

The obtained fields for the temperature and the degree of hydration served as input for the chemomechanical analysis. Based on the original design of the dam, no cracking was encountered during the chemomechanical analysis. In fact, the design of RCC dams aims at a minimization of cracking. The analysis confirmed that this aim was reached. In a second analysis, the cementitious content of RCC was increased whereas the environmental temperature was decreased. The so-obtained increase of the temperature and the temperature gradients in the dam resulted in early-age cracking of RCC. In addition to cracking at the bottom and the upstream and downstream face of the dam, cracking was encountered in the center part of the dam. The distribution of a crack indicator which relates the number of broken hydrates to the number of already-formed hydrates has shown, however, that except from the cracked part at the downstream face of the dam, opened cracks were healed by the ongoing hydration process.

References

[1] Meschke G. Consideration of aging of shotcrete in the context of a 3D viscoplastic material model. Int J Num Meth Eng 1996;39:3123–43.
[2] de Borst R, van den Boogaard A. Finite-element modelling of deformation and cracking in early-age concrete. J Eng Mech 1995;120(12):2519–34.
[3] Niu Y-Z, Tu C-L, Liang R-Y, Zhang S-W. Modelling of thermomechanical damage of early-age concrete. J Eng Mech 1995;121(4):717–26.
[4] Ulm F-J, Coussy O. Modeling of thermochemomechanical couplings of concrete at early ages. J Eng Mech (ASCE) 1995;121(7):785–94.
[5] Ulm F-J, Coussy O. Strength growth as chemo-plastic hardening in early age concrete. J Eng Mech (ASCE) 1996;122(12):1123–32.
[6] Hellmich C, Ulm F-J, Mang HA. Multisurface chemoplasticity. I: Material model for shotcrete. J Eng Mech (ASCE) 1999;125(6):692–701.

[7] Sercombe J, Hellmich C, Ulm F-J, Mang HA. Modeling of early-age creep of shotcrete. I: Model and model parameters. J Eng Mech (ASCE) 2000;126(3):284–91.
[8] Lackner R, Hellmich C, Mang H. Constitutive modeling of cementitious materials in the framework of chemoplasticity. Int J Num Meth Eng 2002;53(10):2357–88.
[9] Cervera M, Oliver J, Prato T. Thermo-chemo-mechanical model for concrete. I: Hydration and aging. J Eng Mech (ASCE) 1999;125(9):1018–27.
[10] De Schutter G, Taerwe L. Fracture energy of concrete at early ages. Mater Struct 1997;30:67–71.
[11] Brameshuber W, Hilsdorf H. Development of strength and deformation of very young concrete, In Shah S, Swartz S, editors. Proceedings of the SEM/RILEM International Conference on Fracture of Concrete and Rock. Houston, Texas, USA: 1987. p. 409–21.
[12] Freiesleben Hansen P, Pedersen E. Måleinstrument til kontrol af betons hardening [Measurement device for controlling hardening of concrete]. Nordisk Betong 1977;1:21–5.
[13] Koiter W. General theorems for elastic–plastic solids, vol. I (Chapter IV). North-Amsterdam: Holland Publishing Company; 1960. p. 167–18.
[14] Bažant Z. Thermodynamics of solidifying or melting viscoelastic material. J Eng Mech Division, ASCE 1979;105(6):933–52.
[15] Mindess S, Young J, Lawrence F-J. Creep and drying shrinkage of calcium silicate pastes. I: Specimen preparation and mechanical properties. Cement Concrete Res 1978;8:591–600.
[16] Catharin P. Hydratationswärme und Festigkeitsentwicklung [Hydration heat and strength evolution], Tech. Rep. 31, Forschungsinstitut des Vereins der österreichischen Zementfabrikanten, Vienna, Austria, In German (October 1978).
[17] Byfors J. Plain concrete at early ages, Tech. rep., Stockholm, Sweden: Swedish Cement and Concrete Research Institute; 1980.
[18] Boumiz A, Vernet C, Cohen Tenoudij F. Mechanical properties of cement pastes and mortars at early age. Adv Cement Based Mater 1996;3:94–106.
[19] Acker P. Comportement mécanique du béton: apports de l'approche physico-chimique [Mechanical behavior of concrete: a physico-chemical approach], Tech. Rep. Res. Rep. LCPC 152, Laboratoires des Ponts et Chaussées, Paris, France, In French, 1988.
[20] Hillerborg A, Modeer M, Petersson P. Analysis of crack formation and crack growth in concrete by means of fracture mechanics and finite elements. Cement Concrete Res 1976;6:773–82.
[21] Neville A. Properties of concrete. third ed. London: Pitman Publishing; 1981.
[22] Editorial, Roller compacted concrete dams, In Water Power and Dam Construction Yearbook. Dartford: Wilmington Business Publ.; 2001. p. 154–60.
[23] Hansen K. Roller compacted concrete dams worldwide. In: Water Power and Dam Construction Handbook. Dartford: Wilmington Business Publ; 1987. p. 27–31.
[24] Dunstan M. Recent developments in roller compacted concrete dam construction. In: Water Power and Dam Construction Handbook. Dartford: Wilmington Business Publ; 1989. p. 39–47.
[25] Sterenberg J. The RCC technique: a perfect integration in the field of gravity dams. Water Power and Dam Construction 1992: 36–8.
[26] Cervera M, Oliver J, Prato T. Simulation of construction of RCC dams. I: temperature and aging. J Struct Eng (ASCE) 2000;126(9):1053–61.
[27] Zhou Y, Rajapakse K, Graham J. Coupled consolidation of a porous medium with a cylindrical or a spherical cavity. Int J Num Anal Meth Geomech 1998;22:449–75.
[28] Acker P, Foucrier C, Malier Y. Temperature related mechanical effects in concrete elements and optimization in the manufacturing process. In: Young J, editor. Concrete at early ages. Detroit: American Concrete Institute (ACI); 1986. p. 33–48.
[29] Rao K, Sastry B, Misra B. A finite element study of geothermal heat flow into coal mine openings. In: Siriwardane H, Zaman M, editors. Computer methods and advances in geomechanics. IACMAG; 1994. p. 1877–82.
[30] Sarkaria G, Andriolo F. Special factors in design of high RCC gravity dams Part II. Water Power and Dam Construction 1995:17–24.